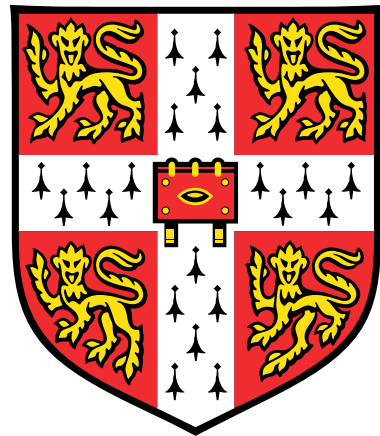


# **Monitoring Vegetation Trends as a Result of Climate Change**



**Panagiotis Antonopoulos**

UNIVERSITY OF CAMBRIDGE

Department of Physics, The Cavendish Laboratory  
Department of Applied Mathematics and Theoretical Physics  
Institute of Astronomy

MPhil in Data Intensive Science

*Supervisor: Dr. Hugo V. Lepage*

## **ABSTRACT**

Monitoring vegetation trends in response to climate change is essential for predicting future impacts on ecosystems, biodiversity, and access to natural resources. Furthermore, reproduction studies are a critical component of the scientific process, helping to verify and strengthen previous findings. In this replication study, I conducted a time series analysis of MODIS EVI data across the Pacific slope of Peru and northern Chile from 2000 to 2024, identifying a statistically significant greening strip consistent with that reported in the original work. To assess how EVI trends relate to climate drivers, I analysed correlations between EVI time series and precipitation, sea surface temperature, and atmospheric CO<sub>2</sub> across various Köppen-Geiger climate zones within both the study area and the greening strip. Finally, I extended the study to California, USA, where I observed widespread vegetation browning (including within national parks), highlighting the broader applicability of this approach.

## **ACKNOWLEDGEMENTS**

*This thesis is dedicated to my family, without whose support and encouragement I would not be where I am today.*

*I would also like to express my deepest gratitude to my supervisor, Dr. Hugo V. Lepage, for his invaluable guidance throughout the project and for providing an exciting research opportunity that I have thoroughly enjoyed.*

# CONTENTS

1	INTRODUCTION	1
2	METHODS	4
2.1	DATA ACQUISITION	4
2.2	DATA PROCESSING	5
2.2.1	UPPER ENVELOPE RECONSTRUCTION	5
2.2.2	TREND DETECTION	6
2.3	CALCULATING CORRELATIONS	8
2.3.1	OUTLINING THE GREENING STRIP	8
2.3.2	SPATIALLY AVERAGING EVI TIME SERIES	8
2.3.3	CLIMATE DRIVERS' TIME SERIES	8
2.3.4	LAGGED CORRELATIONS	9
3	RESULTS	11
3.1	PERU & NORTHERN CHILE	11
3.2	EXTENDED RESULTS - CALIFORNIA, USA	15
4	DISCUSSION	16
4.1	INTERPRETATION OF RESULTS: PERU & NORTHERN CHILE	16
4.2	INTERPRETATION OF EXTENDED RESULTS: CALIFORNIA, USA	19
4.3	DIRECTIONS FOR FURTHER STUDIES	20
5	CONCLUSION	21
	REFERENCES	22

## LIST OF TABLES

1	Correlations between spatially averaged EVI time series for different K-G climate zones within both the full study area and the greening strip (GS), and climate drivers including precipitation, SST, and atmospheric CO <sub>2</sub> concentration. . . . .	14
2	Comparison between the relative correlations within each region from the original work with this study. 'Precip' refers to precipitation and quotes ("") implies repeated entries. . . . .	18

## LIST OF FIGURES

1	Colour coded Köppen-Geiger climate zones. The study area is depicted by the dark shaded region in the inset. Only the BWh, BWk, and BSk regions were considered in this study. Figure taken from [1]. . . . .	2
2	Tiled Region of Interest (ROI) in the MODIS native sinusoidal projection. Blue represents the ROI and red represents the tiles. . . . .	4
3	Illustration of the upper envelope reconstruction including seasonal decomposition for an arbitrary pixel. . . . .	6
4	Flowchart summarising the data processing pipeline. Document shapes represent data, rectangles represent processes, and dashed outlines represent where data are excluded. . . . .	7
5	Flowchart summarising the process to determine correlations. Document shapes represent data, rectangles represent processes, rectangles with rounded corners represent final results, and double barred rectangles represent subroutines. . . . .	10
6	$\Delta_{EVI}$ heatmap overplotted on a satellite image of the study area. The greening strip is outlined in black. . . . .	11
7	A greening gap is observed from approx. 9.6°S to 10.3°S. The top and bottom dashed boxes are the cities of Trujillo and Barranca, respectively, and were excluded from the analysis. . . . .	12
8	The larger and smaller dashed boxes represent the city and province of Lima and Cañete, respectively. The double headed arrow separates greening occurring in the greening strip from coastline greening associated with coastal Lomas [1]. Furthermore, can be seen that the greening increases in intensity southwards from Lima. . . . .	12
9	The solid box shows the Majes irrigation project which exhibits browning due to recent focus shifting to new sites leading to reduced irrigation [1]. The dashed box represents the city of Arequipa. Both are examples of areas excluded from the analysis. . . . .	13
10	Left: The coastal greening is no longer observed. The dashed box with a red line illustrates a road and the one with a green line represents a river, both were excluded from the analysis. Right: Another greening gap is identified between approximately 19.9°S and 20.6°. The dashed box shows a mine or quarry and the greening strip gradually comes to an end. . . . .	13
11	Spatially averaged greening strip EVI time series with each climate driver's time series. . . . .	14
12	$\Delta_{EVI}$ heatmap overplotted on a satellite image of California, USA. . . . .	15
13	GeoTIFFs showing projection artefacts. The red patch in the bottom right corner of each subplot is the Majes irrigation project. . . . .	17



## 1 INTRODUCTION

Climate change is widely recognised as having adverse effects on ecosystems [2–6], which can potentially lead to a loss of biodiversity through the endangerment or extinction of species [7–10]. Beyond biological impacts, ecosystem degradation can also have economic and sociological consequences, as it threatens livelihoods and reduces access to essential natural resources [11]. Monitoring vegetation trends represents a critical approach for assessing the impacts of climate change on ecosystems and contributes to a collective understanding of environmental transformation in response to changing climate drivers.

### *Remote Sensing*

A convenient and widely adopted method for monitoring vegetation trends is through the use of satellite data [12–15]. The Earth Observing System (EOS) Terra and Aqua satellites, launched in 1999 and 2002 respectively, are both equipped with the Moderate Resolution Imaging Spectroradiometer (MODIS) instrument [16]. MODIS is a satellite-based sensor specifically designed to collect data from the Earth's land, oceans, and atmosphere. It measures electromagnetic radiation across 36 spectral bands ranging from 0.405 to 14.385 microns and provides a spatial resolution of up to 250 meters [16]. Existing studies have leveraged MODIS to assess crop yields [17], monitor air quality [18], and detect floods [19]; demonstrating its ability to serve as a versatile tool for environmental monitoring.

### *Vegetation Indices*

A vegetation index is a quantitative measure that indicates the condition of vegetation [20] and is derived by combining surface reflectance values from multiple spectral bands [21]. These indices have been widely employed in studies related to agriculture assessment [22], deforestation monitoring [23], and drought detection [24], as well as for broader applications in environmental monitoring and biodiversity conservation [25]. One commonly used vegetation index is the Normalised Difference Vegetation Index (NDVI), which utilises data from the Near-Infrared (NIR) and red spectral bands. The NDVI is based on the principle that healthy, photosynthesising vegetation absorbs red light and reflects NIR light, whereas unhealthy vegetation exhibits the opposite pattern due to reduced photosynthetic activity [1]. NDVI has found wide applications in assessing tree growth [26], estimating chlorophyll concentrations in leaves [27], and differentiating between ecosystem types [28]. However, studies have noted that NDVI saturates at large biomass values [29] which makes changes in land use and land cover challenging to identify [30]. To address these limitations, MODIS also provides the commonly used Enhanced Vegetation Index (EVI) [31], which builds on NDVI by incorporating blue band data and correction coefficients alongside the red and NIR bands [32]. These additions allow EVI to reduce the influence of soil background and atmospheric aerosols [31,33], while enabling greater sensitivity in densely vegetated and forested areas [32].

### *Köppen-Geiger Climate Zones*

The Köppen-Geiger (K-G) climate classification model aims to identify the climatic factors that influence the types of vegetation found in a given geographical region [1]. With the increasing availability of climate data, successive revisions of the K-G model have enhanced its utility in examining and forecasting the impacts of climate change on global vegetation distributions [34]. The K-G system categorises climates based on temperature and precipitation into five main groups: tropical, arid, temperate, continental, and polar. These groups are further subdivided using seasonal precipitation patterns and temperature thresholds, resulting in thirty distinct climate zones [35]. By grouping regions into ecologically and climatically similar zones, the

## 1 INTRODUCTION

---

K-G system provides a valuable framework for analysing how changes in climate drivers affect the distribution of vegetation across different regions [1, 36].

### *Study Area*

The study area considered in this project is the Pacific slope of the Andes in Peru and northern Chile. The relevant K-G climate zones intersecting this region include the arid hot desert (BWh), the arid cold desert (BWk), and the cold semi-arid steppe (BSk). These climate zones are illustrated in Figure 1 together with the study area.

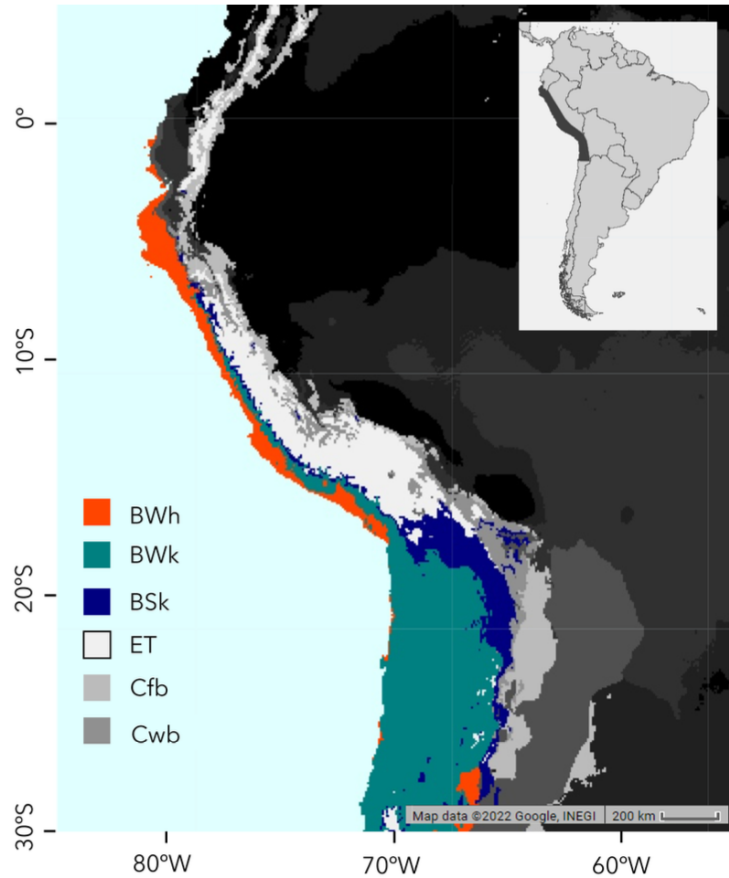


Figure 1: Colour coded Köppen-Geiger climate zones. The study area is depicted by the dark shaded region in the inset. Only the BWh, BWk, and BSk regions were considered in this study. Figure taken from [1].

Previous research has emphasised the need for further investigation on vegetation trends in mountainous regions [37–39]. Additionally, arid areas in particular are highly sensitive to changing climate drivers [40–42], where these effects may be amplified by evapotranspiration [43]. This region was selected as the focus of the study due to its ecological and socio-environmental significance. It is both arid and mountainous [1], characterised by high levels of biological endemism [44–46] and includes largely unmodified natural climate zones [1]. Moreover, the Pacific slope of Peru is considered one of the most water scarce and climate vulnerable areas in South America [47]. Major cities in Peru, such as Lima [48] and Arequipa [49], as well as Antofagasta [50] and Calama [51] in northern Chile depend heavily on the limited natural water resources of this region, placing substantial pressure on the surrounding ecosystems. Consequently, understanding the spatio-temporal response of vegetation to climate change in this region is crucial for predicting the future impacts on ecosystem services, managing resource availability, and conserving endemic species.

### *Review of Existing Studies*

Previous work in this field has monitored vegetation trends in the Ivvavik, Sirmilik, Torngat, and Wapusk National Parks in northern Canada using NDVI values derived from Landsat satellite imagery [52]. The authors reported a consistent greening trend across all parks, attributed to rising temperature patterns. Similarly, data from the Copernicus programme's Sentinel-2 satellite were analysed using Google Earth Engine [53] to conduct a time series analysis of NDVI values in fire-affected areas across Campania, Basilicata, Calabria, Toscana, Umbria, and Lazio in southern Italy [54]. This study examined land use and land cover changes from the year following the fire to the present (at the time of writing) and the utility of NDVI in tracking post-fire vegetation dynamics, including recovery and resilience, was highlighted. The authors found that the integration of Sentinel-2 data with Google Earth Engine facilitated the detection and classification of subtle changes in vegetation at the pixel level (10 m resolution) in burned areas.

MODIS NDVI data have previously been used in time series analyses to study positive and negative vegetation trends (indicating greening and browning, respectively) across a range of locations; from the Northwestern Highlands of Ethiopia [55] to Écrins National Park in the Alps [56], and the entire Himalayan mountain range [57]. These studies commonly employ established techniques such as Savitzky-Golay filtering [58] for smoothing time series data, and Theil-Sen regression [59] to estimate vegetation trends. As the use of EVI has gained popularity over NDVI due to its improved robustness [60], studies geographically closer to the current study area reported observations of dry-season greening in the Amazon rainforest using MODIS EVI time series [61]. These findings were initially contested as an artefact of changes in sun-sensor geometry, specifically, seasonal variations in NIR reflectance [62]. However, subsequent research demonstrated that even after correcting for this artefact, statistically significant greening remained evident and was further supported by ground-based observations [63]. While the Andean region has previously been investigated as part of a broader geographic study spanning from northern Colombia to Argentina [64], the motivations to study the Pacific slope of Peru and northern Chile previously outlined warrant focused investigation.

### *Study Objectives*

The primary objective of this project is to reproduce the results presented in [1], hereafter referred to as the original work. Specifically, the aim is to conduct a time series analysis of MODIS EVI data across the Pacific slope of Peru and northern Chile over a 24-year period (2000-2024), and to identify a statistically significant ‘greening strip’. Additionally, the project aims to correlate spatially averaged EVI time series data for different K-G climate zones within both the study area and the greening strip with climate drivers such as atmospheric CO<sub>2</sub> concentration, Sea Surface Temperature (SST), and precipitation. Although this project is focused on reproducing previous findings, such replication studies are a vital component of the scientific process and support the open science movement. Nevertheless, this project extends the original work by: (i) developing an open source fully contained pipeline in Python, using the Google Earth Engine API to acquire, process, and carry out statistical analysis on the data, (ii) examining another region (California, USA) to demonstrate scalability and generality of the pipeline, and (iii) proposing future work which may build on that presented here.

### *Structure of Report*

This report begins with an introduction to the background theory, along with a review of existing methods in Section 1. Section 2 outlines the methodology used for data acquisition, processing, and calculating correlations with climate drivers. Section 3 presents the results, followed by a critical discussion of the findings in Section 4. Finally, the report concludes in Section 5.

## 2 METHODS

### 2.1 DATA ACQUISITION

To begin the data acquisition process, I used GIS software such as QGIS or Google Earth Pro to manually draw a polygon around the study area, hereafter referred to as the Region of Interest (ROI). This polygon was then exported as a .kml file and compressed into a .zip archive, although it should be noted that exporting it as a .shp file would have also been valid. Next, I created a Google Earth Engine (GEE) project and imported the ROI polygon as a GEE asset, making it accessible via the GEE Python API in a Jupyter Notebook environment. It should be noted that all Jupyter Notebooks used in this project are configured using the `notebook_setup.txt` file contained within the Git repository.

Within the data acquisition notebook, I loaded the ROI geometry and accessed both the EVI and the associated Quality Assessment (QA) layer (which indicates the reliability of EVI values) from the EOS Terra MODIS MOD13Q1 [65] product (version 6.1), which returns 16-day composite images at a 250m spatial resolution [66]. The dataset was filtered to include only images overlapping the ROI and spanning the full duration of the study period. To manage memory limitations and ensure scalable processing, I implemented a tiling strategy to divide the ROI into smaller, more manageable batches. This is because processing the entire dataset at once (comprising millions of pixels over hundreds of time points) would have exceeded available computational resources. Initially, standard rectangular tiling over the ROI introduced edge artefacts at tile boundaries. To avoid this, I opted to generate tiles covering approximately 2,500 km<sup>2</sup> using the native MODIS sinusoidal projection to ensure consistent spatial alignment with the original dataset. This required transforming the ROI to the MODIS projection (SR-ORG:6974), then computing its bounding box by extracting the coordinate extrema. The number of tiles that would fit horizontally and vertically within this bounding box was calculated, and the tiles were generated by iterating through the projected bounding box coordinates to create rectangular geometries in the MODIS projection. Finally, only tiles that intersected the ROI were retained for further processing. An illustration of the tiles is presented below (Figure 2).

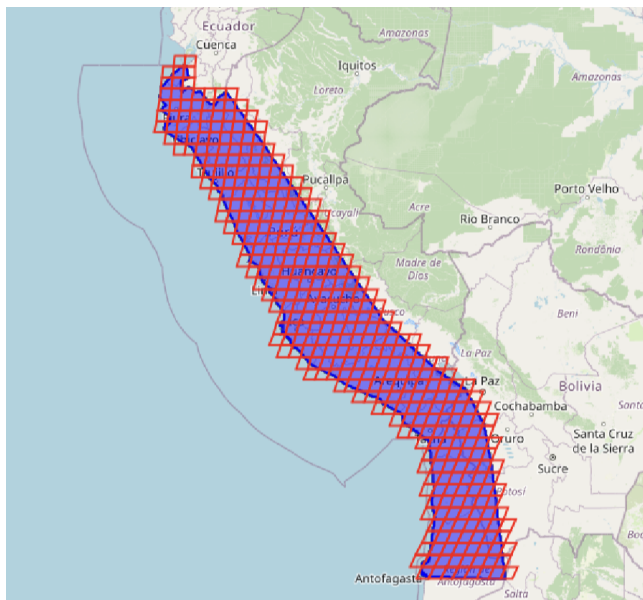


Figure 2: Tiled Region of Interest (ROI) in the MODIS native sinusoidal projection. Blue represents the ROI and red represents the tiles.

Once the tiles were generated, I extracted the full EVI and QA time series for every pixel within each tile and exported them as a .csv file. To do this, I defined a function that, for each tile, filtered the MODIS image collection to include only images intersecting the tile's geometry. I then separately renamed the EVI and QA bands with their corresponding acquisition dates and stacked them to form two time series image stacks before subsequently combining them into a single multiband image. Finally, I extracted all pixel values across all bands (representing the full temporal record of EVI and QA values) and exported them as a .csv file to Google Drive. In the resulting .csv, each row corresponds to a single pixel, and each column represents the EVI or QA value on a specific date.

## 2.2 DATA PROCESSING

To process the raw EVI time series data, I defined a function to handle each .csv tile file individually. This function first reads the file and separates the EVI and QA columns. It also verifies that the associated EVI and QA timestamps are aligned to ensure consistency. For each pixel, EVI values were scaled by a factor of 0.0001 following MODIS documentation [67]. Additionally, pixels were excluded if more than 29.3% of their EVI values were missing over the study period, as Theil-Sen regression loses robustness below this threshold [68].

### *Seasonal Decomposition*

Raw EVI time series exhibit strong seasonal cycles due to natural vegetation dynamics. To isolate long-term trends, I removed seasonality using the `seasonal_decompose` function from the `statsmodels` Python package [69], with a period of 23 (reflecting 16 day composites over one year). Since `seasonal_decompose` does not handle consecutive NaN values well, the time series was first linearly interpolated. It should be noted that apart from the trend, the residual component was also retained, as the default seasonal extraction remove meaningful variation [69].

### 2.2.1 UPPER ENVELOPE RECONSTRUCTION

To preserve and enhance ecologically meaningful EVI peaks while minimising the effect of noise and outliers, I reconstructed the upper envelope of the time series. This approach mitigates spurious depressed EVI values associated with noise or cloud cover.

### *Quality Masking*

To begin the upper envelope reconstruction, I used QA values to mask EVI readings that correspond to invalid observations. Specifically, I masked pixels where QA = -1 (fill value), 2 (snow/ice), or 3 (clouds), consistent with MODIS QA flags [67]. After masking, I excluded any pixels where more than 29.3% of the time series were invalid. This represents a deviation from the method in the original work as snow/ice and cloud contaminated values should be treated as equivalent to missing data due to their inaccuracy.

### *Smoothing and Iterative Fitting*

For valid pixels, the de-seasonalised and interpolated time series was defined as  $N^0$ . I then applied Whittaker smoothing [70] (with  $\lambda = 10$ ) to obtain a smoothed series  $N^{tr}$ , and constructed a new envelope  $N_i^1 = \max(N_i^0, N_i^{tr})$  to suppress any remaining downward spikes typically caused by clouds if any remained after the quality masking. Before iteratively fitting the time series, I computed fitting weights for each data point using Equation 1. These weights were designed to emphasise peaks and suppress troughs, thereby guiding the upper envelope reconstruction to follow the maxima in the signal.

$$W_i = \begin{cases} 1, & \text{when } N_i^0 \geq N_i^{tr} \\ 1 - \frac{d_i}{d_{\max}}, & \text{when } N_i^0 < N_i^{tr} \end{cases} \quad (1)$$

where  $d_i = |N_i^0 - N_i^{tr}|$  and  $d_{\max} = \max(d_i)$  [1].

The iterative fitting procedure (for up to 10 iterations) was then applied. In each iteration, I used the Savitzky-Golay filter (window length = 9, polynomial order = 6) to smooth the envelope,  $N^1$ . A new upper envelope was then defined as  $N_i^k = \max(N_i^0, N_i^{fit})$  where  $N_i^{fit}$  is the result of the Savitzky-Golay filter. Additionally, at each step, a fitting index  $F_k$  was computed [1] to evaluate convergence of the upper envelope fitting by summing over all time series data points using:

$$F_k = \sum_{i=1}^n |N_i^k - N_i^0| \times W_i \quad (2)$$

The iterative fitting continued until the minimum  $F_k$  was found, and I selected the fit corresponding to that value. It should be noted that if the maximum number of iterations was reached before reaching a minimum, the fit from the final iteration was used and if the fitting index increased consistently, the fit from the first iteration was retained. To further reduce noise while preserving trend characteristics, I again smoothed the final envelope using Whittaker smoothing (with  $\lambda = 2$ ). The upper envelope reconstruction is illustrated below (Figure 3) where the progression can clearly be seen.

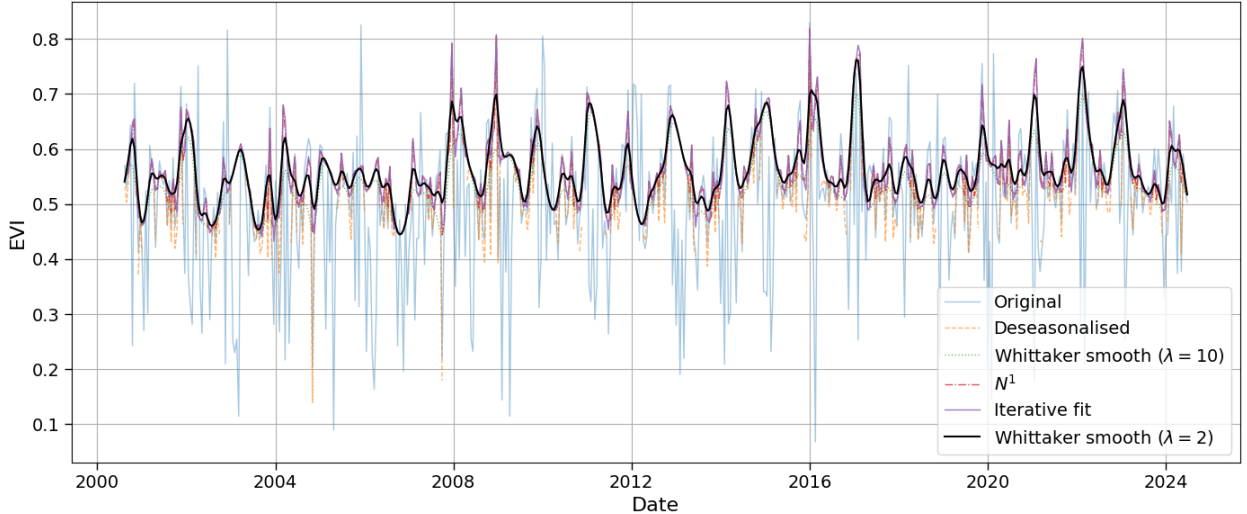


Figure 3: Illustration of the upper envelope reconstruction including seasonal decomposition for an arbitrary pixel.

### 2.2.2 TREND DETECTION

The final smoothed time series was tested for statistically significant trends using the Mann-Kendall test, implemented via the `pymannkendall` Python package. This returned the slope and intercept of the trend (via Theil-Sen and Conover's method, respectively), as well as Kendall's Tau,  $\tau$  and the p-value of the test,  $p$ . A pixel was considered to show a statistically significant trend if  $|\tau| > 0.2$  or  $p < 0.05$ . For those statistically significant pixels, I computed the relative EVI change over the study period,  $\Delta_{EVI}$  using the following formula from [1]:

$$\Delta_{EVI} = \frac{\text{slope} \times \text{len}(\text{time series}) - 1}{\text{intercept} - \text{slope} \times \text{len}(\text{final series})} \quad (3)$$

where 'final series' is the result of the Whittaker smoothing with  $\lambda = 2$ .

The resulting  $\Delta_{EVI}$  values, along with the pixel coordinates (extracted from the .geo column of the raw data), were written to a .json file in GeoJSON format. Finally, the full processing pipeline was executed by iterating over all .csv tile files in the input directory. Each tile was processed individually and its output was saved to the specified output directory.

This process is summarised in the flowchart below (Figure 4), which is adapted from the one in the original work [1].

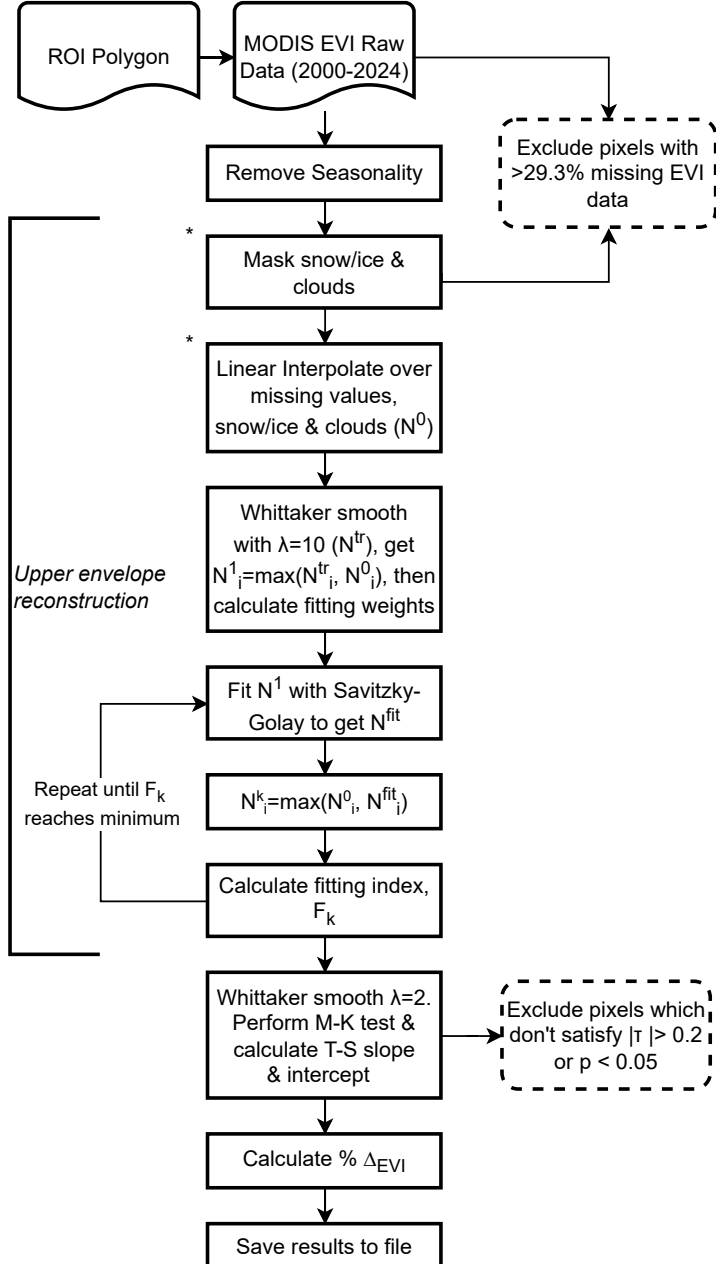


Figure 4: Flowchart summarising the data processing pipeline. Document shapes represent data, rectangles represent processes, and dashed outlines represent where data are excluded.

## 2.3 CALCULATING CORRELATIONS

### 2.3.1 OUTLINING THE GREENING STRIP

Before calculating correlations, I used the Land Cover Classification System (LCCS) [71] to identify and exclude geographic areas corresponding to urban zones, agricultural cropland, and bodies of water. To achieve this, I exported the LCCS .tif file using the Google Earth Engine (GEE) Python API and I then created a GeoDataFrame containing all previously saved EVI data points from Section 2.2. After loading the LCCS raster, which provides discrete land cover classes with associated values, I extracted the land cover class for each EVI point and appended these values to the GeoDataFrame. Specifying which land cover types to exclude, I filtered out any entries corresponding to those classes. Next, I generated a colourised raster image of the filtered  $\Delta_{EVI}$  results and saved it as a GeoTIFF file. Following this, I loaded the GeoTIFF using QGIS and manually created a polygon layer outlining the greening strip (demonstration .gifs illustrating this process are available in the demos directory). This polygon was then exported as a .shp file and imported as a GEE asset, following the same process as originally done for the ROI. Finally, I displayed the delta EVI heatmap with the outline of the greening strip polygon over-plotted for visualisation.

### 2.3.2 SPATIALLY AVERAGING EVI TIME SERIES

#### *Greening Strip Average EVI*

At this point, I used the GEE Python API to compute and export the spatially averaged EVI of all filtered pixels within the greening strip at each time point between 2000 and 2024. This involved loading the raw MODIS MOD13Q1 [65] EVI data for the greening strip and applying the LCCS mask to exclude the previously identified land cover types. The Earth Engine `reduceRegion` function was then used to calculate the mean of all filtered EVI values in the greening strip for each time point, and the resulting data were exported as a .csv file.

#### *K-G Zones Average EVI*

Next, I defined a Python function that utilised the GEE Python API to obtain spatially averaged EVI time series for filtered pixels within the BWh, BWk, and BSk climate zones inside the study area and the greening strip (referred to as GS\_BWh, GS\_BWk, and GS\_BSk). This function followed the same procedure as for the GS itself, but additionally loaded the Köppen-Geiger classification, created a mask for the specified climate zone using its class code [72], and combined it with the LCCS mask. These spatially averaged EVI time series were then processed as described in the data processing section (Section 2.2) and illustrated in the flowchart (Figure 4), with the exception of the asterisked steps. It should also be noted that since the climate drivers' time series were measured monthly, the EVI data were aggregated to monthly means to ensure equal time series lengths and avoid unnecessary data loss.

### 2.3.3 CLIMATE DRIVERS' TIME SERIES

#### *Sea Surface Temperature & Atmospheric CO<sub>2</sub>*

Raw Sea Surface Temperature (SST) data was downloaded from [73]. To maintain consistency with the original work, I constructed the SST time series by averaging the temperature at each time point over a rectangular region bounded by 6°S-30°S latitude and 70°W-80°W longitude. The resulting time series was saved as a .csv file. Following this, atmospheric CO<sub>2</sub> concentration data were downloaded from [74]. The .csv file contained a monthly time series representing the long-term trend, with seasonal variations already removed.

*Greening Strip Average Precipitation*

Monthly mean precipitation data for the greening strip were obtained using the GEE Python API to load the CHIRPS dataset [75], filtered for the duration of the study period. Following this, I defined a Python function to compute the monthly average precipitation over the greening strip for each year. This function defines a second function which calculates the total precipitation over a month, performs a spatial average over the greening strip, and returns the average monthly precipitation for the region. Finally, the outer function returns a list of 12 monthly mean precipitation values. This process was repeated for all years in the study period, and the final time series was exported as a .csv file.

*K-G Zones Average Precipitation*

As with the spatially averaged EVI data, I used a similar approach to obtain precipitation time series for the BWh, BWk, and BSk climate zones within both the full study area and the greening strip. This was done by defining a Python function that applied a Köppen-Geiger climate mask to isolate the desired climate zone before performing the same monthly averaging procedure. It should be noted that both the precipitation and SST time series were seasonally decomposed, with both seasonal and residual components removed. These time series were then smoothed using Whittaker smoothing with  $\lambda = 5$ . The CO<sub>2</sub> time series was neither seasonally decomposed nor smoothed, as it already represented a trend-only series.

## 2.3.4 LAGGED CORRELATIONS

In determining the correlations between the spatially averaged EVI time series and the climate driver time series, I implemented a lagged Spearman correlation function. This approach accounts for the fact that vegetation responses to climate drivers are not instantaneous. Instead of calculating the standard correlation by comparing values at the same time points, the lagged correlation allows for delayed responses by comparing point  $n$  in one time series with point  $n + x$  in the other, where  $x$  represents the lag. The lagged correlation function slides one time series forward or backward by a specified lag and computes the Spearman correlation coefficient at each shift. It iterates over possible lags, from  $-\text{max\_lag}$  to  $+\text{max\_lag}$ , aligning the arrays at each lag and excluding any NaN values before computing the correlation using `np.corrcoef`. The function keeps track of the highest correlation value found across all tested lags and returns this maximum correlation along with its corresponding lag. For this study, I applied the function with a maximum lag of 12 months in both directions for SST and CO<sub>2</sub>, and only 1 month in both directions for precipitation as the study area is primarily populated with vegetation which respond to precipitation in under a month [1].

The full process to determine the correlations is summarised in the flowchart below (Figure 5).

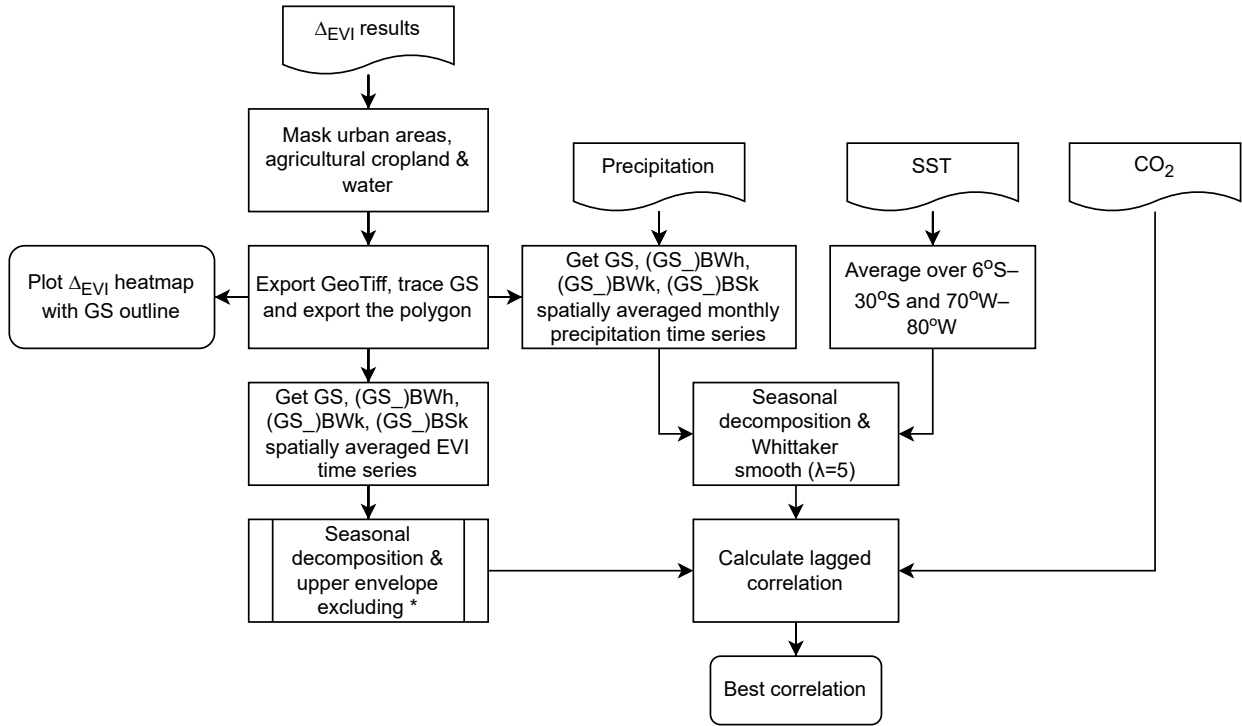


Figure 5: Flowchart summarising the process to determine correlations. Document shapes represent data, rectangles represent processes, rectangles with rounded corners represent final results, and double barred rectangles represent subroutines.

## 3 RESULTS

### 3.1 PERU & NORTHERN CHILE

After conducting the analysis outlined in Section 2 to process the MODIS EVI data for the Pacific slope of Peru and northern Chile from 2000 to 2024, a statistically significant greening strip was identified, as illustrated below (Figure 6). This finding is consistent with the results reported in the original work.

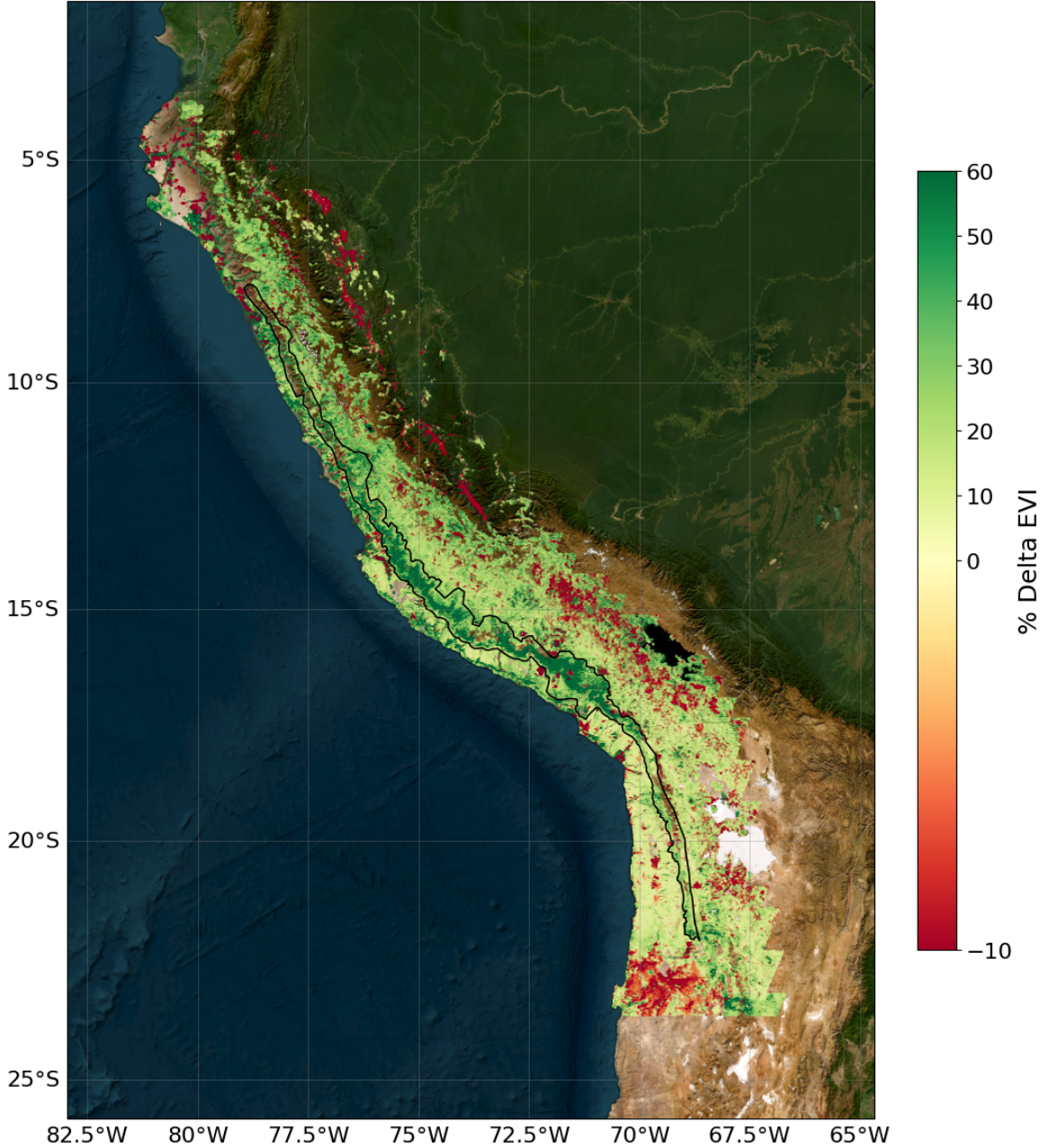


Figure 6:  $\Delta_{EVI}$  heatmap overplotted on a satellite image of the study area. The greening strip is outlined in black.

The heatmap in Figure 6 displays only statistically significant pixels, and the  $\Delta_{EVI}$  values have been clipped to the range of -10% to +60% to reduce the influence of outliers. To examine the heatmap in greater detail, higher resolution images were generated and are presented below (Figures 7-10).

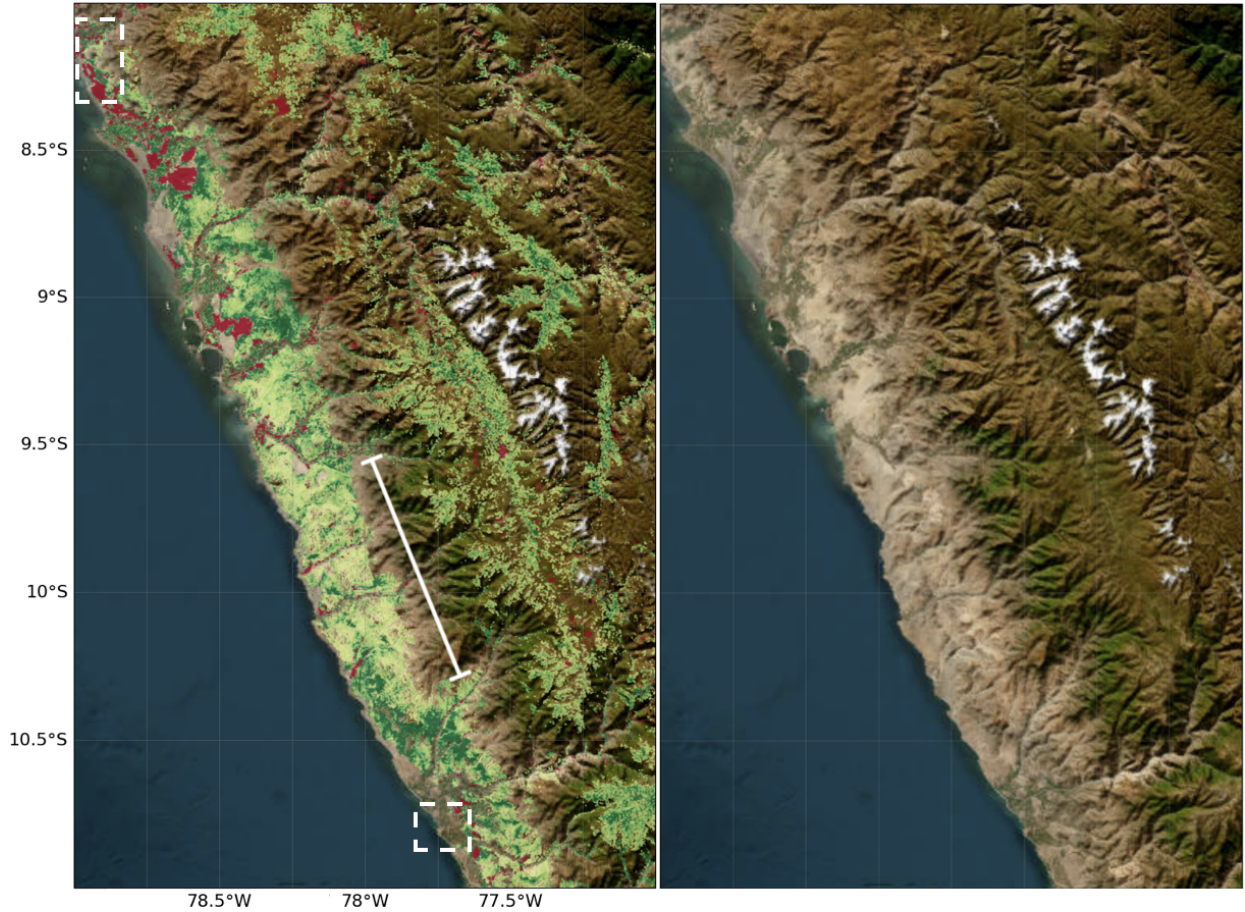


Figure 7: A greening gap is observed from approx.  $9.6^{\circ}\text{S}$  to  $10.3^{\circ}\text{S}$ . The top and bottom dashed boxes are the cities of Trujillo and Barranca, respectively, and were excluded from the analysis.

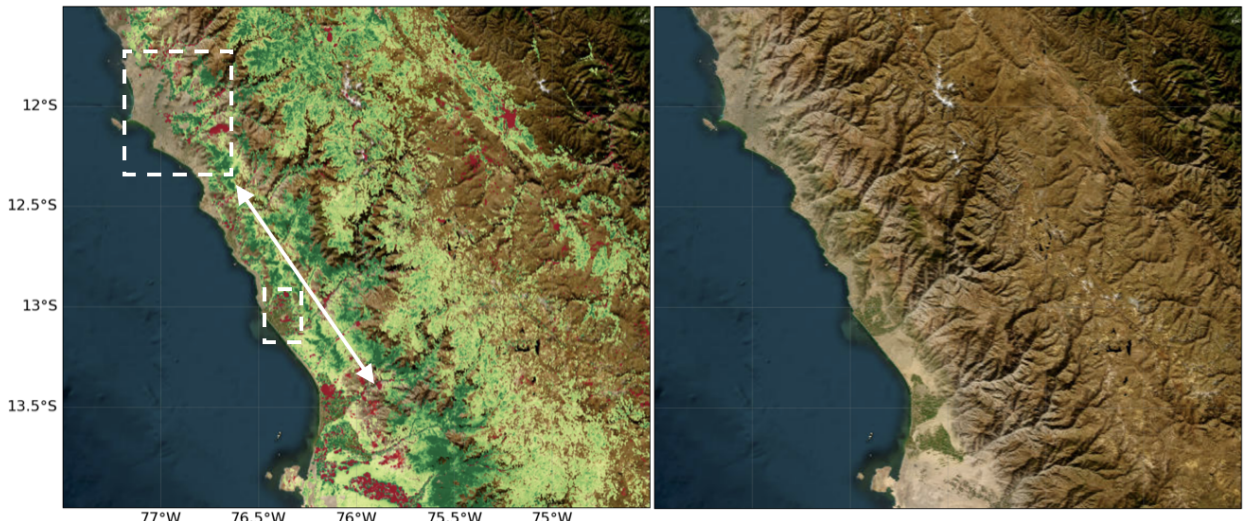


Figure 8: The larger and smaller dashed boxes represent the city and province of Lima and Cañete, respectively. The double headed arrow separates greening occurring in the greening strip from coastline greening associated with coastal Lomas [1]. Furthermore, can be seen that the greening increases in intensity southwards from Lima.

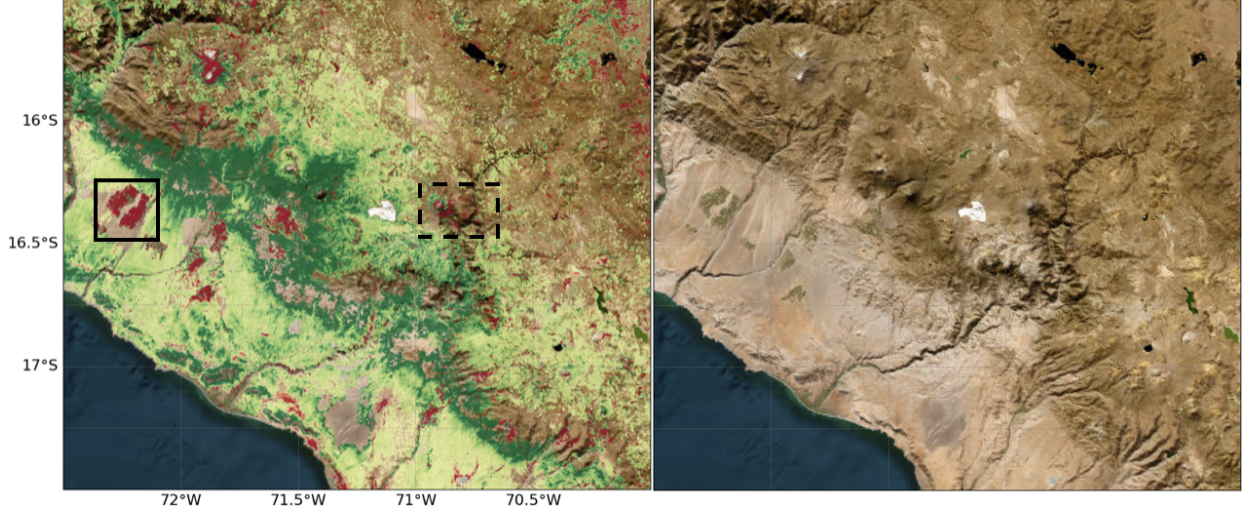


Figure 9: The solid box shows the Majes irrigation project which exhibits browning due to recent focus shifting to new sites leading to reduced irrigation [1]. The dashed box represents the city of Arequipa. Both are examples of areas excluded from the analysis.

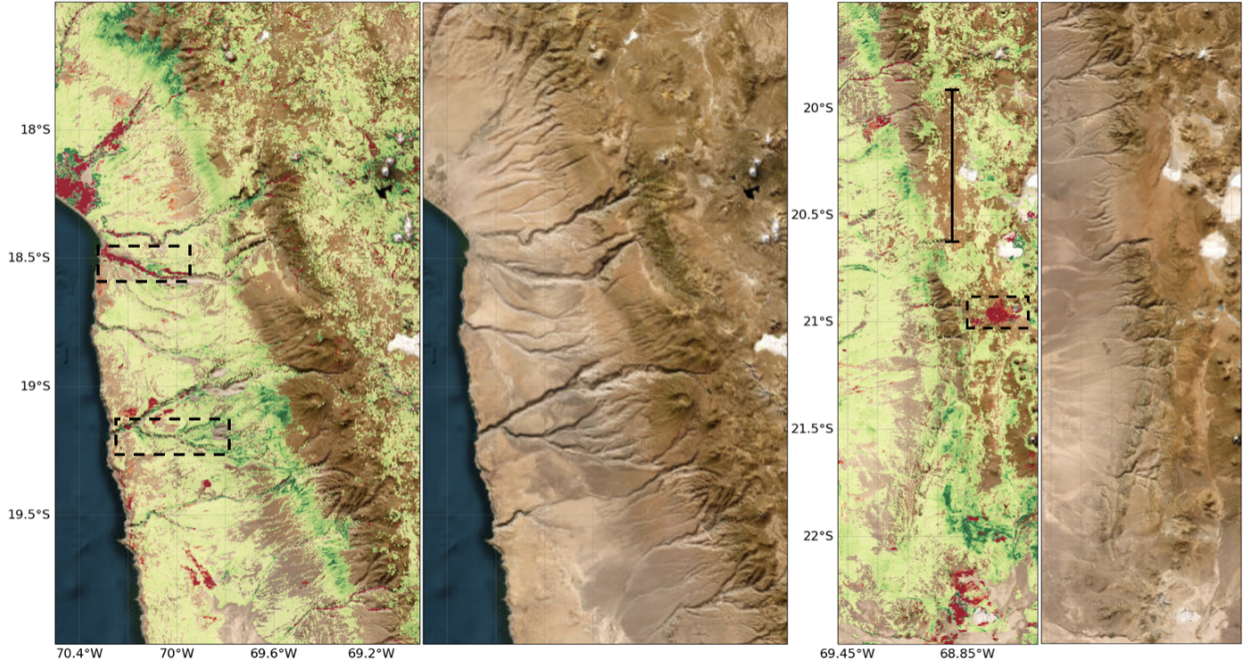


Figure 10: Left: The coastal greening is no longer observed. The dashed box with a red line illustrates a road and the one with a green line represents a river, both were excluded from the analysis. Right: Another greening gap is identified between approximately  $19.9^{\circ}\text{S}$  and  $20.6^{\circ}\text{S}$ . The dashed box shows a mine or quarry and the greening strip gradually comes to an end.

Additionally, following the procedure outlined in Section 2, the correlations between the spatially averaged EVI time series and the climate drivers were computed. These results are presented in Table 1, alongside illustrations of the greening strip EVI time series correlated with each climate driver (Figure 11).

Region	Precipitation	SST	Global CO <sub>2</sub>
BWh	0.39	0.46	0.21
BWk	0.60	0.43	0.47
BSk	0.41	0.29	0.32
GS	0.51	0.43	0.36
GS_BWh	0.50	0.45	0.43
GS_BWk	0.55	0.46	0.36
GS_BSk	0.45	0.38	0.24

Table 1: Correlations between spatially averaged EVI time series for different K-G climate zones within both the full study area and the greening strip (GS), and climate drivers including precipitation, SST, and atmospheric CO<sub>2</sub> concentration.

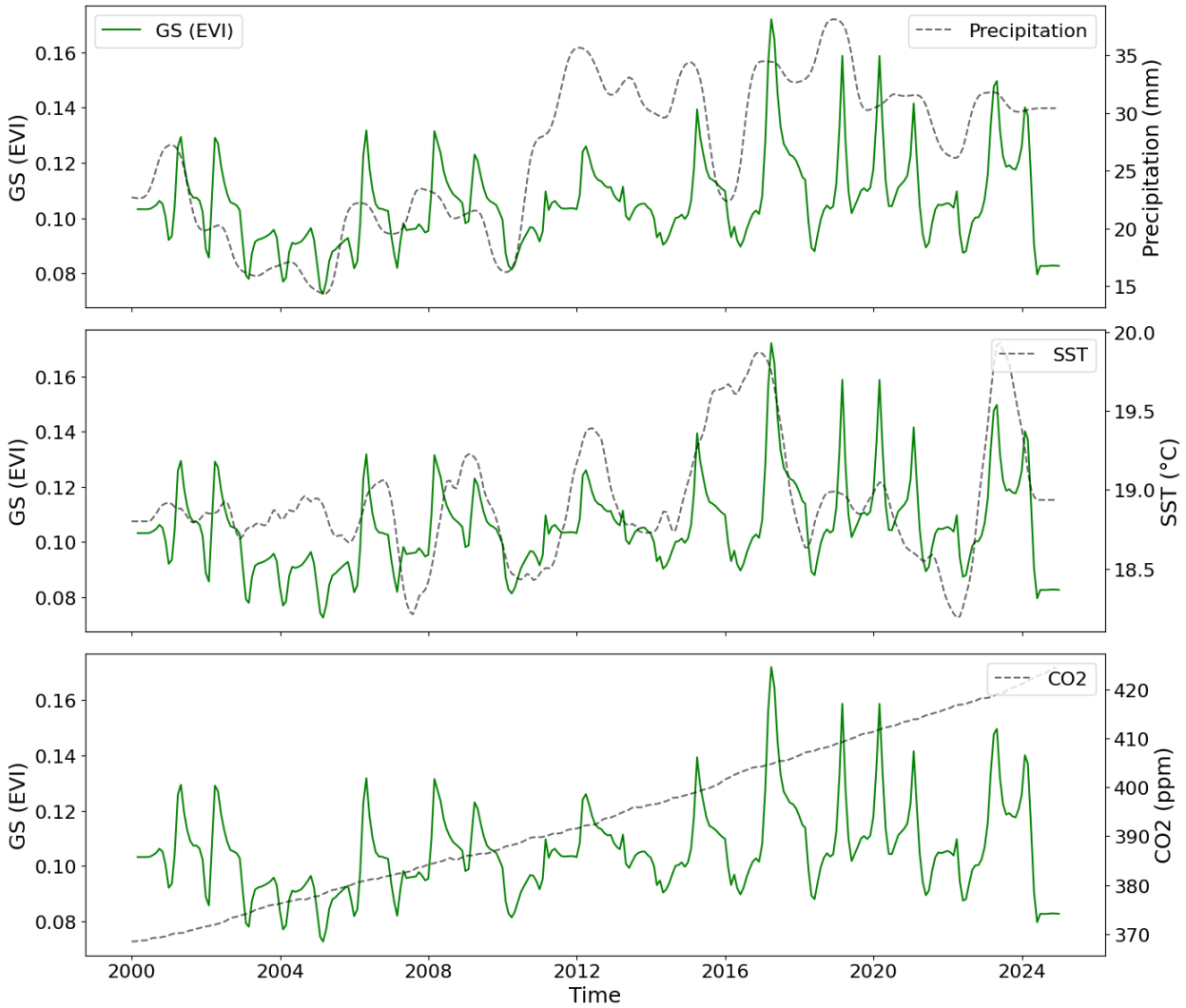


Figure 11: Spatially averaged greening strip EVI time series with each climate driver's time series.

### 3.2 EXTENDED RESULTS - CALIFORNIA, USA

To demonstrate the scalability and generality of the pipeline, a polygon was manually drawn around California, USA, and imported as a GEE asset, as was done with the original study area. The same procedure (excluding correlation calculations) was then executed, and the resulting heatmap is presented below (Figure 12).

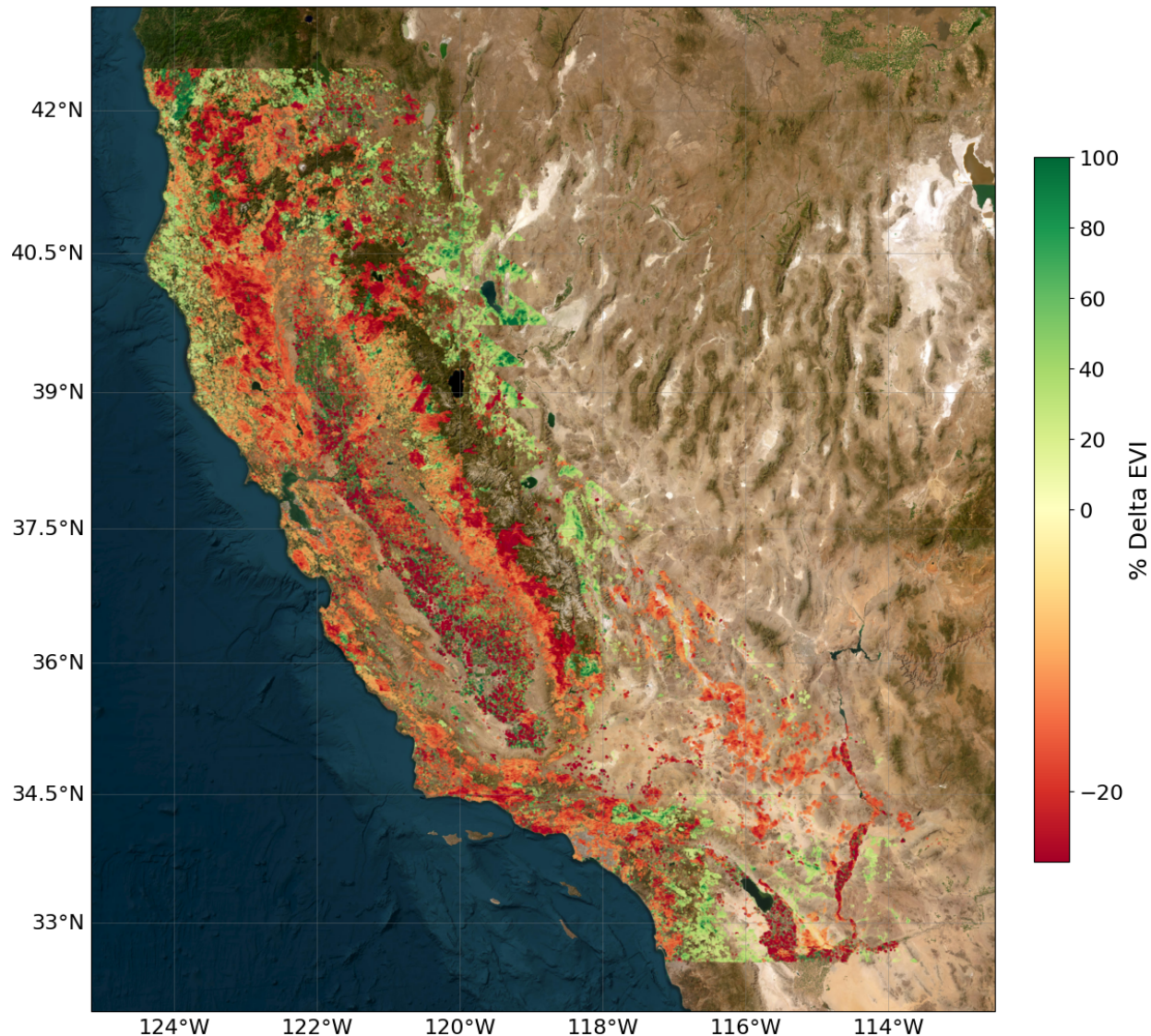


Figure 12:  $\Delta_{EVI}$  heatmap overplotted on a satellite image of California, USA.

## 4 DISCUSSION

### 4.1 INTERPRETATION OF RESULTS: PERU & NORTHERN CHILE

#### *Greening Strip Heatmap*

The heatmap in Figure 6 illustrates a statistically significant greening strip along the Pacific slope of Peru and northern Chile, closely matching the finding of the original work in both location and pattern.

However, Figure 6 improves upon the original image by displaying only statistically significant pixels, rather than all pixels. While the inset in the original work's figure is said to show only statistically significant pixels, this significance was determined based on whether  $\Delta_{EVI}$  exceeded  $\pm 15\%$ . In contrast, the figure presented here assesses statistical significance based on the more robust significance test using Kendall's Tau and the p-value from the Mann-Kendall test (outlined in Section 2.2.2). This refinement enhances the figure's interpretability by excluding non significant data and focusing on areas that exhibit meaningful change. The more 'patchy' appearance results from the exclusion of pixels that either lacked sufficient valid EVI data over the study period or did not show a statistically significant trend. Including such pixels in the figure (for subsequent analysis or data driven decision making) would potentially be misleading.

One notable example that demonstrates the improvement of Figure 6 over the original work's figure is in the region around  $20^{\circ}\text{S}$ ,  $67.5^{\circ}\text{W}$ . In the original figure, two prominent green patches appear, suggesting intense greening in those areas. However, one of these regions corresponds to the Uyuni Salt Flat - the world's largest salt flat, covering approximately  $10,000 \text{ km}^2$  [76]; and the other to the Coipasa Salt Flat. Hence, their apparent greening in the original figure represents a spurious signal that could bias subsequent analysis. Furthermore, these areas also appear in the inset of the original figure which was intended to show only statistically significant greening. This highlights the limitation in the significance criterion used to produce the inset in the original work. In contrast, Figure 6 correctly excludes these salt flats, thereby mitigating the risk of false greening signals and demonstrating the improvement achieved with the refined methodology.

#### *Generated GeoTIFFs*

It can also be seen from Figure 6 that using tiles in the MODIS sinusoidal projection eliminates the edge artefacts between tiles that were present when standard rectangular tiles were used. However, it should be noted that the generated GeoTIFFs exhibited projection artefacts. Several examples of this are presented below (Figure 13). These were identified as projection artefacts because three GeoTIFFs were generated using different projections while all other parameters were held constant. In the first subplot, diagonal bands are visible across the image; in the second subplot, horizontal stripes appear at regular intervals; and in the third subplot, horizontal stripes occur at irregular intervals. Although these artefacts affect the visual appearance of the GeoTIFF, they were not considered a significant issue, as there was no unintended data loss associated with tiling or analysis. This was verified by observing that 'missing' pixels in one subplot were present in another when only the export projection was changed. Moreover, in the centre subplot, some of the horizontal stripes are translucent, allowing the heatmap pixels beneath to remain visible - further confirming that no data was lost. Since the GeoTIFF was used solely to outline the greening strip in QGIS, and the data integrity was preserved, no immediate action was taken to correct this. Nevertheless, future work should investigate these projection artefacts in more detail to generate an artefact free GeoTIFF.

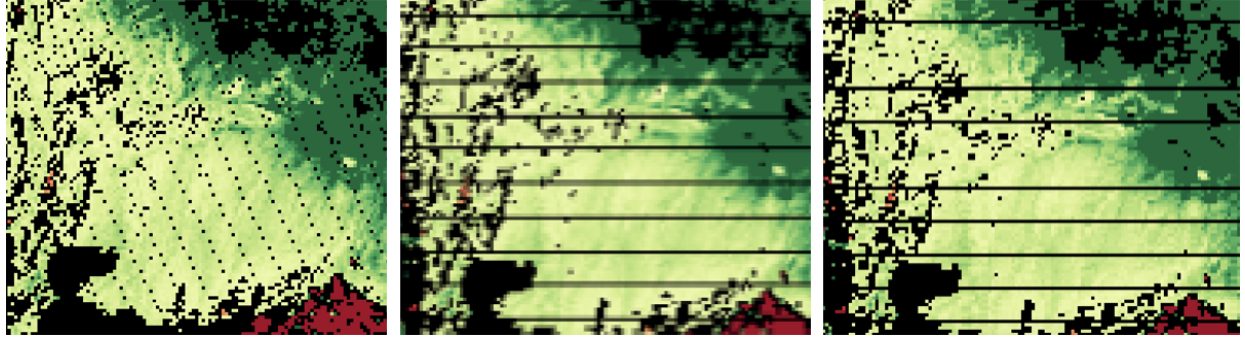


Figure 13: GeoTIFFs showing projection artefacts. The red patch in the bottom right corner of each subplot is the Majes irrigation project.

#### *Higher Resolution Images*

The greening gap observed in Figure 7 is consistent with the gap identified in the original work, appearing in the same location and spanning approximately the same distance. Additionally, the glacier region contains no EVI values, as expected. After applying the QA band to mask snow and ice, this area lacked sufficient valid data and was therefore correctly excluded from the analysis. Notably, the original work shows greening in this glacier region, which likely represents a spurious signal arising from its limitations outlined previously. In this figure, the small red areas are associated with agriculture and were excluded from subsequent analysis, as they reflect non natural vegetation change.

The observation from the original work that greening intensifies southward from Lima is also accurately reproduced in Figure 8, where the greening is visibly stronger toward the bottom of the figure compared to the top, where Lima is located. Additionally, the same separation between the greening strip and coastal greening is observed. These coastal Lomas were excluded from the analysis, as their greening is driven by distinct microclimatic factors and they are geographically distinct from the main greening strip [1]. The observation of a red line crossing the greening strip at approximately  $13^{\circ}\text{S}$ ,  $76.2^{\circ}\text{W}$  matches that made in the original work and represents a road. Similarly, the red spot south-west of this road indicates a mine, which is also reported in the original work. Finally, a key difference between the figure presented here and that of the original work is the absence of EVI values over Lima. This reflects Lima's status as one of the world's cloudiest cities [77, 78]; as a result, when EVI values associated with cloud cover were masked, insufficient valid data remained for those pixels, leading to their exclusion.

As in the original work, Figure 9 accurately depicts the Majes irrigation project west of Arequipa, showing significant browning due to reduced irrigation, alongside a broad area of strong greening. Additionally, more coastal greening is observed in this figure. However, in the left panel of Figure 10, the coastal region at  $18.25^{\circ}\text{S}$ ,  $70.4^{\circ}\text{W}$  (previously shown as greening in the original work) appears to be browning. Upon further investigation, this area is found to be primarily agricultural. While some greening remains visible, the majority of the region shows browning, which could suggest farmland abandonment. Further south, the same roads and rivers highlighted in the original work are also identifiable. Finally, the right panel of Figure 10 shows a second greening gap between  $19.9^{\circ}\text{S}$  and  $20.6^{\circ}\text{S}$ , which appears to have expanded approximately 0.4 degrees southward since the original study. This panel also reproduces the observation of the mine or quarry located south of the greening gap, along with the southern end of the greening strip.

### *Correlations*

This study shows slight differences from the original work in the observed correlations between the spatially averaged EVI time series for different K-G climate zones (both within the overall study area and within the greening strip) and the climate drivers: CO<sub>2</sub> concentration, SST, and precipitation, as presented in Table 1.

While this study supports the original finding that all correlations are positive and EVI correlations with precipitation vary more outside the greening strip than within it, it also generally aligns with the observation that EVI tends to show lower correlation with SST and higher correlation with CO<sub>2</sub> outside the strip compared to inside (although this latter pattern is less pronounced). Notably, the BWh and GS\_BWh regions deviate from this trend, suggesting a different response pattern in this particular K-G zone.

In addition, the relative strengths of the correlations within each region differ. Whereas the original work consistently reported the strongest EVI correlation with CO<sub>2</sub>, this study finds it to be the weakest in all but two regions (BWk and BSk). This comparison is summarised in Table 2.

Region	Original Work	This Study
BWh	CO <sub>2</sub> > Precip > SST	SST > Precip > CO <sub>2</sub>
BWk	”	Precip > CO <sub>2</sub> > SST
BSk	”	Precip > CO <sub>2</sub> > SST
GS	”	Precip > SST > CO <sub>2</sub>
GS_BWh	”	Precip > SST > CO <sub>2</sub>
GS_BWk	”	Precip > SST > CO <sub>2</sub>
GS_BSk	”	Precip > SST > CO <sub>2</sub>

Table 2: Comparison between the relative correlations within each region from the original work with this study. 'Precip' refers to precipitation and quotes (") implies repeated entries.

From Table 2, these differences in relative correlation strengths are evident. However, when considered alongside Table 1, it can be seen that BWh and GS\_BWh have very similar EVI correlations with SST and a similar pattern is observed for the BWk and GS\_BWk regions. Additionally, Figure 1 shows that BWk and GS\_BWk have comparable EVI correlations with precipitation, as do BSk and GS\_BSk. These similarities are expected, given that each pair represents the same K-G climate zone. Finally, it is noted that the relative correlation strengths in the GS, GS\_BWh, GS\_BWk, and GS\_BSk regions are identical. Since none of the full study area K-G zones show this same pattern, this may suggest that the greening strip is subject to unique environmental factors not as prevalent elsewhere.

The discrepancies between the correlations found in this study and those reported in the original work may be attributed to differences in the methodologies used to determine the correlation strengths. While the original work provides some detail on the construction of the EVI time series for each region, it omits certain methodological steps - such as whether the data were aggregated to monthly means to deal with the mismatch in length with the climate driver's data. Similarly, although the sources of the climate driver data are specified, the processing of these time series are not described in substantial detail beyond noting that seasonal decomposition was applied. Hence, it remains unclear whether residuals were retained or if any smoothing or additional processing was performed.

These omissions likely contribute to the observed differences between Figure 11 in this study and the corresponding figure in the original work - particularly for the EVI, precipitation, and SST time series. The CO<sub>2</sub> time series is more consistent between the two studies because the data was already preprocessed to provide just the trend. Additionally, the implementation of the lagged Spearman correlation function likely differs between the two studies. The original work provides minimal detail on its specific implementation, beyond the choice of maximum lag for each climate driver, making direct comparison challenging.

Nevertheless, the results reported in this study appears to be self consistent. This is supported by Figure 11, which shows a larger EVI-precipitation correlation due to the alignment of troughs between 2002 and 2010, and the sharp increase in precipitation corresponding well with subsequent larger peaks in EVI. In contrast, the low EVI-CO<sub>2</sub> correlation can be attributed to the combination of a relatively noisy EVI time series and a very smooth CO<sub>2</sub> series.

## 4.2 INTERPRETATION OF EXTENDED RESULTS: CALIFORNIA, USA

The heatmap in Figure 12 suggests that while the north-east experiences some greening, there is a significant amount of browning occurring in California, USA. This observation is consistent with previous studies, ranging from analyses using Landsat NDVI data to examine vegetation trends during the 2012-2019 drought [79], to studies employing more similar methods (such as using MODIS NDVI data with the Theil-Sen estimator and Mann-Kendall test) to assess browning resulting from the 2012-2016 drought [80], as well as over a broader period from 2000 to 2017 [81]. However, while these studies typically only reported browning in Southern California, the result presented in Figure 12 suggests vegetation browning is not only localised to the south but occurs throughout the state.

To further investigate the browning observed in California, the locations of various national parks were overlaid on Figure 12, as shown below (Figure 14). While some pixels within the national park boundaries are missing (either due to insufficient valid EVI data or lack of statistical significance) it is evident that many of these protected areas are experiencing browning. This trend is particularly concerning for nature conservation efforts and the preservation of biodiversity in the region. Hence, further studies of this region should specifically investigate the vegetation trends of California's national parks.

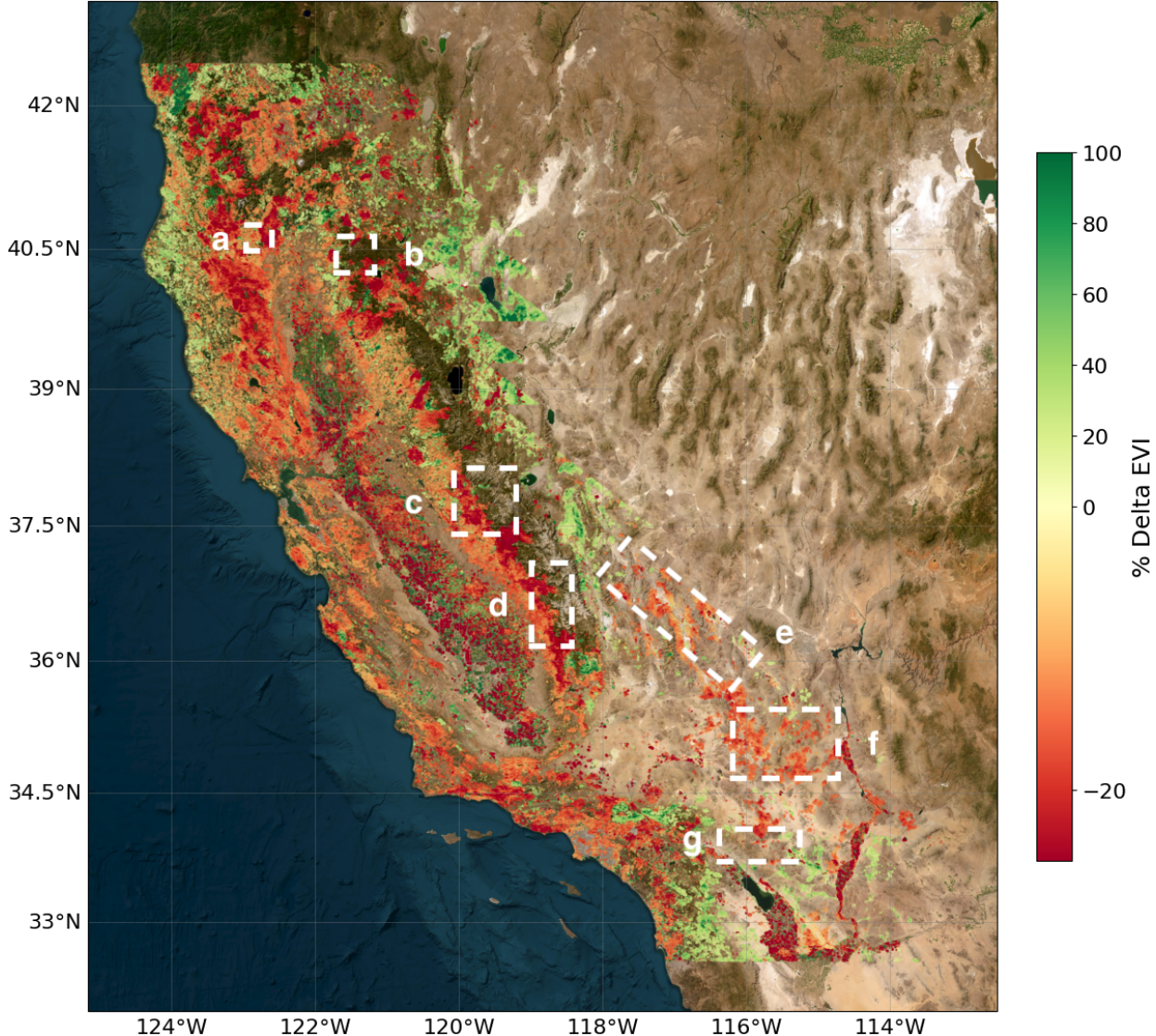


Figure 14:  $\Delta_{EVI}$  heatmap of California, USA with various national parks indicated. a) Whiskeytown-Shasta-Trinity National Recreation Area, b) Lassen Volcanic National Park, c) Yosemite National Park, d) Kings Canyon National Park & Sequoia National Park, e) Death Valley National Park, f) Mojave National Preserve, g) Joshua Tree National Park.

### 4.3 DIRECTIONS FOR FURTHER STUDIES

An immediate direction for future research building on this work would be to apply the pipeline to study additional regions, with the long term goal of generating a global  $\Delta_{EVI}$  heatmap. This would facilitate rapid identification of areas experiencing significant greening or browning. Although the analysis pipeline is open source (with all relevant files available in the accompanying Git repository), it could be further developed into a Python package, making it easily installable via package managers such as `pip` by the scientific community.

Further enhancements to the pipeline could involve integrating data from additional satellite platforms, such as Landsat and Sentinel-2, to supplement the MODIS EVI time series. For instance, missing MODIS EVI values could be replaced using EVI data derived from these alternative sources. This could be achieved by logging the timestamps and geographic locations of

missing EVI data, then checking whether suitable replacement values are available from the other datasets. Incorporating such data may increase pixel retention in the analysis, thereby reducing the ‘patchiness’ currently observed in  $\Delta_{EVI}$  heatmaps.

While the current pipeline is designed with computational efficiency in mind (leveraging GEE cloud resources and tiling the study area), additional improvements could be achieved through processing multiple tiles in parallel using multithread processing as there is no data dependency in the analysis of individual tiles. This could be done by leveraging libraries such as OpenMP [82] in a high performance computing environment.

## 5 CONCLUSION

This study has successfully achieved its primary objective. A statistically significant greening strip was identified through time series analysis of MODIS EVI data across the Pacific slope of Peru and northern Chile, covering the period from 2000 to 2024. This greening strip closely aligns with the one reported in the original work. Additionally, spatially averaged EVI time series were computed for different K-G climate zones within both the broader study area and the greening strip. Their correlations with precipitation, SST, and atmospheric CO<sub>2</sub> concentration were then analysed. While some aspects of the relative correlation strengths agreed with the original findings, the results presented here were self consistent, and any discrepancies were discussed and attributed to methodological differences.

To demonstrate the scalability and generality of the developed pipeline, the analysis was extended to the state of California, USA, following the same procedure. The results revealed significant browning across the state, including within its national parks. This finding is broadly aligned with previous studies but also suggests that the extent of vegetation decline may be more widespread than previously reported. Finally, directions for further research were proposed, aimed at refining the analysis pipeline and enhancing the collective understanding of global vegetation dynamics.

Remote sensing methods such as those used in this study are vital for monitoring vegetation trends and understanding their response to changing climate drivers. This research contributes to an important field that informs policymaking on ecosystem conservation, biodiversity protection, and sustainable resource management.

## REFERENCES

- [1] H. V. Lepage, E. Barnes, E. Kor, M. Hunter, and C. H. Barnes, “Greening and browning trends on the pacific slope of peru and northern chile,” *Remote Sensing*, vol. 15, no. 14, p. 3628, 2023.
- [2] M. L. Asmus, J. Nicolodi, L. S. Anello, and K. Gianuca, “The risk to lose ecosystem services due to climate change: A south american case,” *Ecological Engineering*, vol. 130, pp. 233–241, 2019.
- [3] N. B. Grimm, F. S. Chapin III, B. Bierwagen, P. Gonzalez, P. M. Groffman, Y. Luo, F. Melton, K. Nadelhoffer, A. Pairis, P. A. Raymond *et al.*, “The impacts of climate change on ecosystem structure and function,” *Frontiers in Ecology and the Environment*, vol. 11, no. 9, pp. 474–482, 2013.
- [4] Y. Malhi, J. Franklin, N. Seddon, M. Solan, M. G. Turner, C. B. Field, and N. Knowlton, “Climate change and ecosystems: threats, opportunities and solutions,” p. 20190104, 2020.
- [5] O. Hoegh-Guldberg and J. F. Bruno, “The impact of climate change on the world’s marine ecosystems,” *Science*, vol. 328, no. 5985, pp. 1523–1528, 2010.
- [6] M. N. Gebeyehu and F. H. Hirpo, “Review on effect of climate change on forest ecosystem,” *Int. J. Environ. Sci. Nat. Resour.*, vol. 17, no. 4, pp. 126–129, 2019.
- [7] H. Mooney, A. Larigauderie, M. Cesario, T. Elmquist, O. Hoegh-Guldberg, S. Lavorel, G. M. Mace, M. Palmer, R. Scholes, and T. Yahara, “Biodiversity, climate change, and ecosystem services,” *Current opinion in environmental sustainability*, vol. 1, no. 1, pp. 46–54, 2009.
- [8] D. W. Sintayehu, “Impact of climate change on biodiversity and associated key ecosystem services in africa: a systematic review,” *Ecosystem health and sustainability*, vol. 4, no. 9, pp. 225–239, 2018.
- [9] A. El-Keblawy, “Impact of climate change on biodiversity loss and extinction of endemic plants of arid land mountains,” *J Biodivers Endanger Species*, vol. 2, no. 120, p. 2, 2014.
- [10] B. Gallardo and D. C. Aldridge, “Evaluating the combined threat of climate change and biological invasions on endangered species,” *Biological Conservation*, vol. 160, pp. 225–233, 2013.
- [11] O. D. Elisha and M. J. Felix, “The loss of biodiversity and ecosystems: a threat to the functioning of our planet, economy and human society,” *International Journal of Economics, Environmental Development and Society*, vol. 1, no. 1, pp. 30–44, 2020.
- [12] K. Didan, “Multi-satellite earth science data record for studying global vegetation trends and changes,” in *Proceedings of the 2010 international geoscience and remote sensing symposium, Honolulu, HI, USA*, vol. 2530, 2010, p. 2530.
- [13] E. Honeck, R. Castello, B. Chatenoux, J.-P. Richard, A. Lehmann, and G. Giuliani, “From a vegetation index to a sustainable development goal indicator: Forest trend monitoring using three decades of earth observations across switzerland,” *ISPRS International Journal of Geo-Information*, vol. 7, no. 12, p. 455, 2018.

- [14] A. Hoscilo, H. Balzter, E. Bartholomé, M. Boschetti, P. A. Brivio, A. Brink, M. Clerici, and J.-F. Pekel, “A conceptual model for assessing rainfall and vegetation trends in sub-saharan africa from satellite data,” *International Journal of Climatology*, vol. 35, no. 12, pp. 3582–3592, 2015.
- [15] Q. Zhao, L. Yu, Z. Du, D. Peng, P. Hao, Y. Zhang, and P. Gong, “An overview of the applications of earth observation satellite data: impacts and future trends,” *Remote Sensing*, vol. 14, no. 8, p. 1863, 2022.
- [16] C. Justice, J. Townshend, E. Vermote, E. Masuoka, R. Wolfe, N. Saleous, D. Roy, and J. Morisette, “An overview of modis land data processing and product status,” *Remote sensing of Environment*, vol. 83, no. 1-2, pp. 3–15, 2002.
- [17] P. C. Doraiswamy, T. R. Sinclair, S. Hollinger, B. Akhmedov, A. Stern, and J. Prueger, “Application of modis derived parameters for regional crop yield assessment,” *Remote sensing of environment*, vol. 97, no. 2, pp. 192–202, 2005.
- [18] K. D. Hutchison, “Applications of modis satellite data and products for monitoring air quality in the state of texas,” *Atmospheric Environment*, vol. 37, no. 17, pp. 2403–2412, 2003.
- [19] R. Brakenridge and E. Anderson, “Modis-based flood detection, mapping and measurement: the potential for operational hydrological applications,” in *Transboundary floods: reducing risks through flood management*. Springer, 2006, pp. 1–12.
- [20] A. Bannari, D. Morin, F. Bonn, and A. Huete, “A review of vegetation indices,” *Remote sensing reviews*, vol. 13, no. 1-2, pp. 95–120, 1995.
- [21] R. D. Jackson and A. R. Huete, “Interpreting vegetation indices,” *Preventive veterinary medicine*, vol. 11, no. 3-4, pp. 185–200, 1991.
- [22] J. L. Hatfield, J. H. Prueger, T. J. Sauer, C. Dold, P. O'brien, and K. Wacha, “Applications of vegetative indices from remote sensing to agriculture: Past and future,” *Inventions*, vol. 4, no. 4, p. 71, 2019.
- [23] A. R. Huete, “Vegetation indices, remote sensing and forest monitoring,” *Geography Compass*, vol. 6, no. 9, pp. 513–532, 2012.
- [24] F. N. Kogan, “Application of vegetation index and brightness temperature for drought detection,” *Advances in space research*, vol. 15, no. 11, pp. 91–100, 1995.
- [25] J. Xue and B. Su, “Significant remote sensing vegetation indices: A review of developments and applications,” *Journal of sensors*, vol. 2017, no. 1, p. 1353691, 2017.
- [26] S. M. Vicente-Serrano, J. J. Camarero, J. M. Olano, N. Martín-Hernández, M. Peña-Gallardo, M. Tomás-Burguera, A. Gazol, C. Azorin-Molina, U. Bhuyan, and A. El Kenawy, “Diverse relationships between forest growth and the normalized difference vegetation index at a global scale,” *Remote Sensing of Environment*, vol. 187, pp. 14–29, 2016.
- [27] J. Pastor-Guzman, P. M. Atkinson, J. Dash, and R. Rioja-Nieto, “Spatiotemporal variation in mangrove chlorophyll concentration using landsat 8,” *Remote sensing*, vol. 7, no. 11, pp. 14 530–14 558, 2015.

- [28] N. Pettorelli, J. O. Vik, A. Mysterud, J.-M. Gaillard, C. J. Tucker, and N. C. Stenseth, “Using the satellite-derived ndvi to assess ecological responses to environmental change,” *Trends in ecology & evolution*, vol. 20, no. 9, pp. 503–510, 2005.
- [29] S. Huang, L. Tang, J. P. Hupy, Y. Wang, and G. Shao, “A commentary review on the use of normalized difference vegetation index (ndvi) in the era of popular remote sensing,” *Journal of Forestry Research*, vol. 32, no. 1, pp. 1–6, 2021.
- [30] A. R. Huete, H. Liu, and W. J. van Leeuwen, “The use of vegetation indices in forested regions: issues of linearity and saturation,” in *IGARSS'97. 1997 IEEE international geoscience and remote sensing symposium proceedings. Remote sensing-a scientific vision for sustainable development*, vol. 4. IEEE, 1997, pp. 1966–1968.
- [31] Z. Li, X. Li, D. Wei, X. Xu, and H. Wang, “An assessment of correlation on modis-ndvi and evi with natural vegetation coverage in northern hebei province, china,” *Procedia Environmental Sciences*, vol. 2, pp. 964–969, 2010.
- [32] A. Huete, K. Didan, T. Miura, E. P. Rodriguez, X. Gao, and L. G. Ferreira, “Overview of the radiometric and biophysical performance of the modis vegetation indices,” *Remote sensing of environment*, vol. 83, no. 1-2, pp. 195–213, 2002.
- [33] B. D. Wardlow, S. L. Egbert, and J. H. Kastens, “Analysis of time-series modis 250 m vegetation index data for crop classification in the us central great plains,” *Remote sensing of environment*, vol. 108, no. 3, pp. 290–310, 2007.
- [34] M. Kottek, J. Grieser, C. Beck, B. Rudolf, and F. Rubel, “World map of the köppen-geiger climate classification updated,” *Meteorologische Zeitschrift*, vol. 15, pp. 259–263, 05 2006.
- [35] W. Koppen, “Klassifikation der klimate nach temperatur, niederschlag und jahreslauf,” *Pet. Mitt.*, vol. 64, pp. 193–203, 1918.
- [36] H. E. Beck, N. E. Zimmermann, T. R. McVicar, N. Vergopolan, A. Berg, and E. F. Wood, “Present and future köppen-geiger climate classification maps at 1-km resolution,” *Scientific data*, vol. 5, no. 1, pp. 1–12, 2018.
- [37] J. Krishnaswamy, R. John, and S. Joseph, “Consistent response of vegetation dynamics to recent climate change in tropical mountain regions,” *Global change biology*, vol. 20, no. 1, pp. 203–215, 2014.
- [38] B. Wang, G. Xu, P. Li, Z. Li, Y. Zhang, Y. Cheng, L. Jia, and J. Zhang, “Vegetation dynamics and their relationships with climatic factors in the qinling mountains of china,” *Ecological Indicators*, vol. 108, p. 105719, 2020.
- [39] Y. Kidane, R. Stahlmann, and C. Beierkuhnlein, “Vegetation dynamics, and land use and land cover change in the bale mountains, ethiopia,” *Environmental monitoring and assessment*, vol. 184, pp. 7473–7489, 2012.
- [40] S. Kumar, A. Raizada, H. Biswas, S. Srinivas, and B. Mondal, “Application of indicators for identifying climate change vulnerable areas in semi-arid regions of india,” *Ecological indicators*, vol. 70, pp. 507–517, 2016.
- [41] M. Beuhler, “Potential impacts of global warming on water resources in southern california,” *Water Science and Technology*, vol. 47, no. 7-8, pp. 165–168, 2003.

- [42] R. Loehman, “Understanding the science of climate change: Talking points-impacts to arid lands,” *Natural Resource Report NPS/NRPC/NRR-2010/209. Fort Collins, CO: US Department of the Interior, National Park Service, Natural Resource Program Center.* 35 p., 2010.
- [43] X. Zhang, M. Li, Z. Ma *et al.*, “Evapotranspiration variability over global arid and semi-arid regions from 1982 to 2011,” *Chinese Journal of Atmospheric Sciences*, vol. 42, no. 2, pp. 251–267, 2018.
- [44] E. Barnes, M. A. Hunter, H. V. Lepage, H. E. V. Luján, and N. C. Jamanca, “The avifauna of the río fortaleza drainage basin, dptos. lima and ancash, peru,” *Cotinga*, vol. 44, pp. 43–59, 2022.
- [45] B. Best and M. Kessler, *Biodiversity and conservation in Tumbesian Ecuador and Peru*. International Council for Bird Preservation, 1995.
- [46] A. J. Stattersfield, “Endemic bird areas of the world-priorities for biodiversity conservation,” *Bird Life International*, 1998.
- [47] L. Beagley, G. Bell, M. Smith, J. Hawker, and J. Parker, “Water management and ecosystem services: Peru management guide,” *EO4cultivar Project. UK Space Agency International Partnership Programme*, 2020.
- [48] A. A. Ioris, “Water scarcity and the exclusionary city: the struggle for water justice in lima, peru,” in *Hydrosocial Territories and Water Equity*. Routledge, 2017, pp. 300–314.
- [49] G. Salmoral, E. Zegarra, I. Vázquez-Rowe, F. González, L. Del Castillo, G. R. Saravia, A. Graves, D. Rey, and J. W. Knox, “Water-related challenges in nexus governance for sustainable development: Insights from the city of arequipa, peru,” *Science of the Total Environment*, vol. 747, p. 141114, 2020.
- [50] M. C. Fragkou and J. McEvoy, “Trust matters: Why augmenting water supplies via desalination may not overcome perceptual water scarcity,” *Desalination*, vol. 397, pp. 1–8, 2016.
- [51] C. Herrera, L. Godfrey, J. Urrutia, E. Custodio, T. Jordan, J. Jódar, K. Delgado, and F. Barrenechea, “Recharge and residence times of groundwater in hyper arid areas: The confined aquifer of calama, loa river basin, atacama desert, chile,” *Science of the Total Environment*, vol. 752, p. 141847, 2021.
- [52] R. Fraser, I. Olthof, M. Carrière, A. Deschamps, and D. Pouliot, “Detecting long-term changes to vegetation in northern canada using the landsat satelliteimage archive,” *Environmental Research Letters*, vol. 6, no. 4, p. 045502, 2011.
- [53] N. Gorelick, “Google earth engine,” in *EGU general assembly conference abstracts*, vol. 15. American Geophysical Union Vienna, Austria, 2013, p. 11997.
- [54] R. Lasaponara, N. Abate, C. Fattore, A. Aromando, G. Cardettini, and M. Di Fonzo, “On the use of sentinel-2 ndvi time series and google earth engine to detect land-use/land-cover changes in fire-affected areas,” *Remote Sensing*, vol. 14, no. 19, p. 4723, 2022.
- [55] B. Alemayehu, J. Suarez-Minguez, J. Rosette, and S. A. Khan, “Vegetation trend detection using time series satellite data as ecosystem condition indicators for analysis in the northwestern highlands of ethiopia,” *Remote Sensing*, vol. 15, no. 20, p. 5032, 2023.

- [56] B. Z. Carlson, M. C. Corona, C. Dentant, R. Bonet, W. Thuiller, and P. Choler, “Observed long-term greening of alpine vegetation—a case study in the french alps,” *Environmental Research Letters*, vol. 12, no. 11, p. 114006, 2017.
- [57] N. B. Mishra and K. P. Mainali, “Greening and browning of the himalaya: Spatial patterns and the role of climatic change and human drivers,” *Science of the Total Environment*, vol. 587, pp. 326–339, 2017.
- [58] A. Savitzky and M. J. Golay, “Smoothing and differentiation of data by simplified least squares procedures.” *Analytical chemistry*, vol. 36, no. 8, pp. 1627–1639, 1964.
- [59] P. K. Sen, “Estimates of the regression coefficient based on kendall’s tau,” *Journal of the American statistical association*, vol. 63, no. 324, pp. 1379–1389, 1968.
- [60] Y. Zhang, C. Song, L. E. Band, G. Sun, and J. Li, “Reanalysis of global terrestrial vegetation trends from modis products: Browning or greening?” *Remote Sensing of Environment*, vol. 191, pp. 145–155, 2017.
- [61] A. R. Huete, K. Didan, Y. E. Shimabukuro, P. Ratana, S. R. Saleska, L. R. Hutyra, W. Yang, R. R. Nemani, and R. Myneni, “Amazon rainforests green-up with sunlight in dry season,” *Geophysical research letters*, vol. 33, no. 6, 2006.
- [62] D. C. Morton, J. Nagol, C. C. Carabajal, J. Rosette, M. Palace, B. D. Cook, E. F. Vermote, D. J. Harding, and P. R. North, “Amazon forests maintain consistent canopy structure and greenness during the dry season,” *Nature*, vol. 506, no. 7487, pp. 221–224, 2014.
- [63] S. R. Saleska, J. Wu, K. Guan, A. C. Araujo, A. Huete, A. D. Nobre, and N. Restrepo-Coupe, “Dry-season greening of amazon forests,” *Nature*, vol. 531, no. 7594, pp. E4–E5, 2016.
- [64] T. M. Aide, H. R. Grau, J. Graesser, M. J. Andrade-Nuñez, E. Aráoz, A. P. Barros, M. Campos-Cerqueira, E. Chacon-Moreno, F. Cuesta, R. Espinoza *et al.*, “Woody vegetation dynamics in the tropical and subtropical andes from 2001 to 2014: Satellite image interpretation and expert validation,” *Global change biology*, vol. 25, no. 6, pp. 2112–2126, 2019.
- [65] NASA/METI/AIST/Japan Spacesystems and U.S./Japan ASTER Science Team, “ASTER Global Digital Elevation Model V003,” <https://doi.org/10.5067/ASTER/ASTGTM.003>, 2019, nASA EOSDIS Land Processes Distributed Active Archive Center. Accessed 2025-06-10.
- [66] C. Munyati, “Relating urban land surface temperature to vegetation leafing using thermal imagery and vegetation indices,” *Earth Science Informatics*, pp. 1–18, 2024.
- [67] K. Didan and A. Barreto-Muñoz, “Modis collection 6.1 (c61) vegetation index product user guide,” *The University of Arizona, Vegetation Index and Phenology Lab: Tucson, AZ, USA*, 2019.
- [68] P. J. Rousseeuw and A. M. Leroy, *Robust regression and outlier detection*. John wiley & sons, 2003.
- [69] S. Seabold and J. Perktold, “Statsmodels: econometric and statistical modeling with python.” *SciPy*, vol. 7, no. 1, pp. 92–96, 2010.

- [70] E. T. Whittaker, “On a new method of graduation,” *Proceedings of the Edinburgh Mathematical Society*, vol. 41, pp. 63–75, 1922.
- [71] M. Buchhorn, M. Lesiv, N.-E. Tsendlbazar, M. Herold, L. Bertels, and B. Smets, “Copernicus global land cover layers—collection 2,” *Remote Sensing*, vol. 12, no. 6, p. 1044, 2020.
- [72] H. E. Beck, T. R. McVicar, N. Vergopolan, A. Berg, N. J. Lutsko, A. Dufour, Z. Zeng, X. Jiang, A. I. van Dijk, and D. G. Miralles, “High-resolution (1 km) köppen-geiger maps for 1901–2099 based on constrained cmip6 projections,” *Scientific data*, vol. 10, no. 1, p. 724, 2023.
- [73] H. Hersbach, B. Bell, P. Berrisford, G. Biavati, A. Horányi, J. Muñoz Sabater, J. Nicolas, C. Peubey, R. Radu, I. Rozum, D. Schepers, A. Simmons, C. Soci, D. Dee, and J.-N. Thépaut, “ERA5 monthly averaged data on single levels from 1940 to present,” Copernicus Climate Change Service (C3S) Climate Data Store (CDS), 2023, accessed on 10-06-2025.
- [74] X. Lan, P. Tans, and K. W. Thoning, “Trends in globally-averaged co2 determined from noaa global monitoring laboratory measurements,” <https://doi.org/10.15138/9N0H-ZH07>, 2025, version 2025-06.
- [75] C. Funk, P. Peterson, M. Landsfeld, D. Pedreros, J. Verdin, S. Shukla, G. Husak, J. Rowland, L. Harrison, A. Hoell, and J. Michaelsen, “The climate hazards infrared precipitation with stations—a new environmental record for monitoring extremes,” *Scientific Data*, vol. 2, p. 150066, 2015.
- [76] R. Sieland, “Hydraulic investigations of the salar de uyuni, bolivia,” 2014.
- [77] Geodiode, “City of fog — the climate of lima, peru,” <https://geodiode.com/lima/>, 2011, accessed June 20, 2025.
- [78] S. Kinuthia, “The cloudiest cities in the world,” <https://www.worldatlas.com/articles/cities-who-receive-the-least-sunshine.html>, May 2019, accessed June 20, 2025.
- [79] M. M. Warter, M. B. Singer, M. O. Cuthbert, D. Roberts, K. K. Caylor, R. Sabathier, and J. Stella, “Drought onset and propagation into soil moisture and grassland vegetation responses during the 2012–2019 major drought in southern california,” *Hydrology and Earth System Sciences*, vol. 25, no. 6, pp. 3713–3729, 2021.
- [80] C. Dong, G. M. MacDonald, K. Willis, T. W. Gillespie, G. S. Okin, and A. P. Williams, “Vegetation responses to 2012–2016 drought in northern and southern california,” *Geophysical Research Letters*, vol. 46, no. 7, pp. 3810–3821, 2019.
- [81] C. Dong, G. MacDonald, G. S. Okin, and T. W. Gillespie, “Quantifying drought sensitivity of mediterranean climate vegetation to recent warming: A case study in southern california,” *Remote Sensing*, vol. 11, no. 24, p. 2902, 2019.
- [82] R. Chandra, *Parallel programming in OpenMP*. Morgan kaufmann, 2001.